Journal of Materials Chemistry A

ROYAL SOCIETY OF CHEMISTRY

PAPER

View Article Online
View Journal | View Issue

Cite this: J. Mater. Chem. A, 2022, 10, 8334

Designed synthesis of MOR zeolites using gemini-type bis(methylpyrrolidinium) dications as structure directing agents and their DME carbonylation performance†

Nan Chen,[ab] Jin Zhang,[ab] Yating Gu,[ab] Wenna Zhang,[a] Kaipeng Cao,[ab] Wenhao Cui,[ab] Shutao Xu,[a] Dong Fan,*[a] Peng Tian*[a] and Zhongmin Liu[ab]

Received 17th January 2022
Accepted 2nd March 2022

DOI: 10.1039/d2ta00451h

rsc.li/materials-a

Mordenite (MOR) zeolite is an efficient catalyst for dimethyl ether (DME) carbonylation and syngas to ethylene conversion due to the unique confinement effect and catalytic activity in 8-membered ring (8-MR) side pockets. Herein, aiming at enhancing the distribution of acid sites in the side pockets of MOR and developing high-performance catalysts, a series of bulky gemini-type bis(methylpyrrolidinium) dications with varying methylene chain lengths (*n*BMPr) were designed and proved to be efficient OSDAs for MOR zeolite. The synthesis efficacy of *n*BMPr was revealed to be closely related with the methylene chain lengths. Compared with conventional MOR templated by tetraethylammonium hydroxide (TEAOH), *n*BMPr-MOR possessed an obviously enhanced Brønsted acid distribution and amounts in the side pockets, likely due to the higher charge compensation ability of *n*BMPr for the framework $[AlO_4]^-$ of 12-MR, promoting the preferential location of Na^+ in the side pockets. Consequently, the resultant MOR zeolites showed remarkable catalytic activity in the DME carbonylation reaction. The space-time yield of methyl acetate can reach as high as 12.5 mmol g^{-1} h^{-1}, which is the highest value ever reported for DME carbonylation using zeolitic catalysts.

Introduction

Zeolites are crystalline aluminosilicates with well-defined intrinsic pores and cavities which find wide applications in gas separation and catalysis.[1–3] For zeolite synthesis, the participation of organic structure-directing agents (OSDAs) is commonly indispensable, especially when zeolites with medium/high silica content are targeted. The OSDAs are crucial for the nucleation and crystallization of zeolites, as they can offer a vital stabilization effect for the formation of zeolite frameworks. *Via* the judicious choice of OSDAs, important performance-relevant properties of zeolites, such as morphology, acidity and elemental compositions, can be effectively tailored.[4] Developing new OSDAs for targeted zeolites is key for an insightful understanding of the relationship between zeolite properties and OSDAs, and would shed light on the rational design and synthesis of zeolites.

Recently, DME carbonylation over zeolite catalysts has aroused considerable interest,[5–9] as it provides an effective route to improve the value of C1 chemicals. Methyl acetate (MeOAc), the highly selective product of DME carbonylation, can be used as a solvent for resins. It can also be hydrogenated to produce ethanol, an important chemical and ideal fuel additive. Mordenite is so far the most efficient zeolite catalyst for DME carbonylation. The framework of mordenite is characterized by 12-membered ring channels (12-MR, 6.5 × 7.0 $Å^2$) along the *c* axis direction and interconnected 8-MR side pockets (3.4 × 4.8 $Å^2$) along the *b* axis direction. The Brønsted acid sites (BASs) located in the side pockets have been proven both experimentally and theoretically to be the authentic active centers for DME carbonylation, mainly due to the unique space-confinement effect in the side pockets. The 12-MR main channels, nevertheless, are vulnerable to quick coke deposition from DME/methanol to hydrocarbon reaction, resulting in the blockage of channels and quick catalyst deactivation. Their distinct catalytic behaviors illustrate that regulating the distribution/number of BASs in the 12-MR and 8-MR channels should be an effective approach for tuning the performance of the catalysts.

Hitherto, although the acid distribution of zeolites (closely related with the Al siting) has been recognized as an important parameter affecting the catalytic performance, the relevant

[a]National Engineering Laboratory for Methanol to Olefins, Dalian National Laboratory for Clean Energy, Dalian Institute of Chemical Physics, Chinese Academy of Sciences, Dalian 116023, China. E-mail: fandong08@dicp.ac.cn; tianpeng@dicp.ac.cn

[b]University of Chinese Academy of Sciences, Chinese Academy of Sciences, Beijing 100049, China

† Electronic supplementary information (ESI) available. See DOI: 10.1039/d2ta00451h

research is mainly limited to a few zeolites.[10–13] It has been revealed that the type of OSDA, inorganic cation, hetero-atom substitution, and gel Si/Al ratio (SAR) all have an effect on the Al location. Among them, tuning the OSDAs might be the most effective strategy, as their sizes and structures can be readily tailored, facilitating the adjustment of their locations in the channels and the host–guest interactions with the framework, and thus the manipulating of Al siting. Nevertheless, for the synthesis of MOR zeolite, the reservoir of eligible OSDAs[14–18] is rather limited with TEAOH and hexamethyleneimine (HMI) as the most frequently employed ones. Recently, Huang *et al.* reported the increase of BAS distribution in the 8-MR of MOR by a Ce-incorporation strategy with TEAOH as the OSDA.[19] They also found that the competition between Na^+ and a protonated cyclic amine (such as HMI) in compensating framework charges may play a decisive role in the Al distribution of low silica MOR (SAR = 7–8).[19] Overall, the understanding of the mechanism of OSDA in regulating the Al (acid) distribution of MOR zeolite needs to be improved. The abundance of effective OSDAs would help promote the understanding of this issue.

Aluminosilicate zeolite syntheses employing pyrrolidine-based gemini-type dications as efficient OSDAs have been reported recently (ITQ-39, TNU-9, IM-5 and IWR),[20–23] suggesting their flexibility and versatility in the structure-directed formation of different zeolite topologies. Besides, in an independent ongoing work by us, we found that *N*-methylpyrrolidine is capable of directing the crystallization of MOR zeolite. Herein, a series of bulky gemini-type bis(methylpyrrolidinium) dications with varying methylene chain lengths were rationally designed for the synthesis of MOR (named *n*BMPr-MOR). The template efficacy of *n*BMPr was found to be closely related with the length of the methylene chain. Moreover, the OSDA location and BAS distribution of the materials were thoroughly characterized and their catalytic performance in the DME carbonylation reaction was investigated.

Experimental section

OSDA synthesis

The OSDAs employed in this work consist of two *N*-methylpyrrolidine charged moieties spaced by a linear bridging methylene group (Fig. 1). The doubly charged OSDAs (*n*BMPr, *n* = 2, 3, 4 or 5) were synthesized by reaction of 1-methylpyrrolidine with the corresponding linear dibromoalkane $Br(CH_2)_nBr$. A typical synthesis process (exemplified by the synthesis of 3BMPr) is as follows. Firstly, 85.15 g (1.0 M) 1-methylpyrrolidine was dissolved in 200 mL MeCN. 0.48 M dibromopropane was subsequently added to a round bottom flask equipped with a condenser and kept under reflux at 85 °C for 72 h. After removal of MeCN under vacuum, the bromide salt was obtained and washed with petroleum ether 3 times until the remaining salt was dried. The purity of the dibromide salts described above was confirmed by ^{13}C NMR (Fig. S1†) and stored in a desiccator prior to their use.

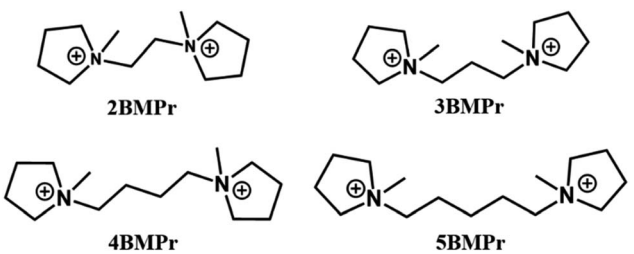

Fig. 1 Illustration of the OSDA structures used in this work.

Zeolite synthesis

A typical zeolite synthesis process is as follows. Sodium hydroxide (NaOH, 98 wt%), sodium aluminate (Al_2O_3, 47.61 wt%; Na_2O, 36.59 wt%) and deionized H_2O were first mixed and stirred intensely at room temperature. After the mixture had dissolved completely, silica sol (SiO_2, 27.34%) and commercial MOR (ZR CATALYST Co., Ltd) as seed crystals (6 wt% relative to SiO_2) were added and the mixture underwent further agitation for another 30 min. Finally, the OSDAs prepared above were added into the mixture. After being stirred at room temperature for 2 h, the synthesized mixture was charged into a 50 mL autoclave and heated at 180 °C for 2–5 days under static conditions. The final composition of the synthesized mixtures was $100SiO_2 : xNa_2O : yAl_2O_3 : 12OSDA : 1500H_2O$, where x is varied in the range $16 \leq x \leq 24$, and y is varied in the range $2.5 \leq y \leq 5$. After crystallization, the resulting solids were collected and washed with distilled water, recovered by centrifugation and dried at 120 °C overnight. To remove the OSDA, the as-made samples were calcined in dry air at 550 °C for 6 h.

The resultant samples were transformed into their proton-type (H-MOR) by ion exchange with 1 M NH_4Cl solution at 80 °C 3 times, followed by further calcination at 550 °C for 6 h in dry air. To prepare Na-MOR with complete Na^+ coverage, the calcined MOR sample was ion-exchanged with 1 M $NaNO_3$ solution three times at 80 °C for 1 h.

In addition, for comparison, MOR zeolite synthesized by using TEAOH (35 wt%) as the OSDA was also prepared according to a previous study.[9] The SAR of the material (named TEAOH-MOR) is 12.1, derived from XRF, and the powder XRD patterns of the TEAOH-MOR reference and MOR seed samples are presented in Fig. S2.†

Analytical methods

X-ray diffraction (XRD) patterns were recorded on a PANalytical X' Pert PRO X-ray diffractometer with Cu Kα radiation (λ = 0.154059 nm) at 40 kV and 40 mA. The elemental compositions of the samples were analyzed using a Philips Magix-601 X-ray fluorescence (XRF) spectrometer. The crystal morphologies were recorded on a Hitachi SU8020 scanning electron microscope (SEM). An SDT650 TA analyzer was used for thermogravimetric analysis (TGA) from room temperature to 900 °C at a heating rate of 10 °C min^{-1} under an air atmosphere (100 mL min^{-1}). The N_2 sorption isotherms were measured on a Micromeritics ASAP 2020 analyzer. Based on the Brunauer–Emmett–Teller (BET) method, the total surface area was

calculated. The micropore volume and area were derived using a *t*-plot method. Temperature-programmed desorption of ammonia (NH_3-TPD) analysis was performed on a Micromeritics Autochem II 2920 equipped with a thermal conductivity detector (TCD). The H-MOR samples (100 mg) were pretreated at 450 °C for 60 min in a helium flow, and then exposed to ammonia for certain period at 100 °C. The desorption process was carried out from 100 to 700 °C. The amounts of organic moieties occluded in the as-made zeolites were determined by CHN elemental analysis using an Elementar vario EL CUBE analyzer. Fourier transform infrared (FTIR) spectra were recorded on a Nicolet IS50 FTIR spectrometer equipped with an MCT detector. The self-supported sample wafers (10 mg) were placed in a quartz cell and pretreated at 300 °C for 1 h under vacuum, and the spectrum of the fresh sample was recorded immediately after the pretreatment. For NH_3-FTIR, NH_3 was introduced into the cell at 100 °C until saturation, followed by an evacuation at different temperatures for 30 min, and the spectra were recorded at 50 °C. The extinction coefficients for the bands at 1440 cm^{-1} (BASs) and 1620 cm^{-1} (LASs) are 0.147 and 0.022 cm^2 μmol^{-1}, respectively.[24] For pyridine-FTIR, the adsorption of pyridine was carried out at 100 °C, followed by an evacuation at different temperatures for 30 min and the spectra were recorded at room temperature.

The liquid ^{13}C NMR experiment was performed on a Bruker Avance III 400 spectrometer using D_2O as a deuterating reagent. The solid-state ^{29}Si, ^{27}Al and ^{23}Na MAS NMR experiments were carried out on a Bruker Avance NEO 500 spectrometer equipped with a 3.2 mm HFXY probe with a spinning rate of 20 kHz. ^{1}H–^{29}Si CP MAS NMR spectra were recorded using a 3.2 mm HFXY probe with a spinning rate of 10 kHz. The ^{1}H–^{13}C CP MAS NMR experiment was performed using a 4 mm WVT HXY probe with a spinning rate of 12 kHz. The resonance frequencies of ^{23}Na, ^{27}Al, ^{29}Si and ^{13}C are 132.2 MHz, 130.3 MHz, 99.3 MHz and 125.8 MHz, respectively. Before the ^{23}Na MAS NMR measurement, the Na-exchanged 2BMPr-MOR sample was pretreated at 400 °C for 12 h to remove the physiosorbed water and other samples were dehydrated at 180 °C for 12 h. Chemical shifts for ^{29}Si, ^{23}Na, ^{27}Al and ^{13}C were referenced to kaolinite (−91.5 ppm), 1 M $NaNO_3$ solution (0 ppm), 1 M $Al(NO_3)_3$ solution (0 ppm) and adamantane (1.74 ppm), respectively.

Computational details

Theoretical calculations were carried out using the Gaussian 09 package based on Density Functional Theory (DFT).[25] The structure information of mordenite was taken from the International Zeolite Association's database, and a 128T cluster ($Si_{128}O_{218}H_{76}$) was extracted and used as the host model. Note that the pure siliceous model was used to simplify the simulation. The combined theoretical ONIOM method[26,27] was applied to optimize the docking sites and structures of the guest organic templates. During optimization, the framework atoms constituting the 12-MR main channel and the guest organic templates were calculated in the high-level layer, while the rest of the atoms were kept in the low-level layer. The ωB97XD hybrid density functional with 6-31G(d,p) basis sets, which implicitly accounts for empirical dispersion and can well describe long-range dispersion interactions with respect to the traditional DFT methods, was utilized for optimization of the high-level layer.[28] The low-level layer optimization was carried out using the semi-empirical AM1 method. All the atoms except for the terminal H atoms were relaxed during the structure optimization.

Catalysis test

DME carbonylation evaluation was performed in a high-pressure fixed-bed reactor. The H-MOR catalyst (0.2 g, 40–60 mesh) was dehydrated in N_2 at 300 °C for 1 h. Afterwards, the reactor temperature was reduced to 275 °C, a pyridine–N_2 mixture (30 mL min^{-1}) was introduced and the reactor was purged for 30 min, which was followed by flushing with N_2 for 1 h. Eventually, the reactor was cooled and maintained at 200 °C. A gas mixture (DME/CO/N_2 = 5/35/60) was introduced into the reactor at a gas hourly space velocity (GHSV) of 7200 or 12 000 mL g^{-1} h^{-1}. The total pressure was 2.0 MPa. Product analysis was carried out using an Agilent 7890B gas chromatograph equipped with a Pora PLOT Q capillary column and FID.

Results and discussion

Summary of zeolite synthesis results

Table S1† summarizes the synthesis protocols and the corresponding product phases obtained using the gemini-type bis(-methylpyrrolidinium) dications with varying methylene spacer length (*n*BMPr, *n* = 2, 3, 4, 5) as crystallization OSDAs. In each case, the products listed were the only ones obtained in repeated trials. The overall synthesis results reveal that the crystallization of MOR is strongly affected by the methylene spacer lengths of the employed OSDAs. Specifically, when 4BMPr or 5BMPr with a longer spacer length is used, longer crystallization duration and higher gel alkalinity are required for the successful crystallization of the MOR phase, accompanied by a low solid yield and narrowed product SAR window. In contrast, pure MOR zeolite could be readily prepared with wider SAR compositions and high solid yields, utilizing 2BMPr or 3BMPr as the OSDA. Moreover, it is noted that the choice of crystallization duration is also key to the MOR synthesis, since zeolite crystallization is in fact a kinetics-controlled process. Longer crystallization duration inevitably results in the transformation of zeolite topology of low framework density to that of a higher one, which is more stable from a thermodynamic point of view.

When the syntheses using 2BMPr and 3BMPr are compared, slightly faster crystallization kinetics and wider phase stabilization duration could be discerned for the 2BMPr system (gel SAR = 15). Compared with 2BMPr and 3BMPr, although an inferior structure-directing ability was evident for 4BMPr, a pure MOR phase with SAR as high as 12.1 could still be achieved by adjusting the alkalinity or increasing the crystallization duration. In contrast, with regard to 5BMPr, the highest SAR that could be reached is only 9.6, despite the variation of alkali/silica ratios, Si/Al ratios and crystallization time. Besides,

transformation from the MOR phase to other phases is more favored with 5BMPr than with 4BMPr. These findings suggest that, compared with 5BMPr, 4BMPr is more effective in hindering the phase transformation and hence has a better structure directing ability for the MOR phase. The ability of the four OSDAs in directing the crystallization of MOR zeolites can be summarized as 2BMPr > 3BMPr > 4BMPr > 5BMPr.

Characterization of MOR zeolites

Four representative MOR samples synthesized with *n*BMPr (n = 2, 3, 4, 5) were selected to undergo a series of characterization experiments. The bulk SARs of the samples are derived from XRF and calculated to be 12.0, 11.9, 12.1 and 9.6 for 2BMPr-MOR, 3BMPr-MOR, 4BMPr-MOR and 5BMPr-MOR, respectively. The powder XRD patterns of the samples are presented in Fig. 2a. The well-resolved diffraction peaks could all be indexed to the MOR phase, suggesting the good purity and crystallinity of the prepared materials. SEM images (Fig. S3†) show that 2BMPr-MOR and 3BMPr-MOR are nanocrystal aggregates with no well-defined shapes. With 4BMPr as the OSDA, plate-like crystals with a thickness of around 100–200 nm were observed. When using 5BMPr as the OSDA, the product shows packed cards-like morphology with regular arrangements of plate-like crystals. N_2 sorption analysis results are displayed in Fig. 2b. The isotherms of all the samples can be considered as composites of type I and type IV isotherms. Obvious hysteresis loops appeared for samples 2BMPr-MOR, 3BMPr-MOR and 5BMPr-MOR, likely due to the stacking voids of nanoaggregates. Table 1 summarizes the derived textural properties of H-MOR samples. The micropore surface areas are in the range of 318–367 $m^2\ g^{-1}$ and the micropore volumes of the samples are in the range of 0.16–0.18 $cm^3\ g^{-1}$, confirming the good crystallinity of the prepared samples.

Table 1 Textural properties of the H-MOR samples

	Surface area[a] ($m^2\ g^{-1}$)			Pore volume[b] ($cm^3\ g^{-1}$)		
Sample	S_{BET}	S_{micro}	S_{ext}	V_{total}	V_{micro}	V_{meso}
2BMPr-MOR	374	334	40	0.21	0.16	0.05
3BMPr-MOR	365	325	40	0.21	0.16	0.05
4BMPr-MOR	344	318	26	0.18	0.16	0.02
5BMPr-MOR	432	367	65	0.27	0.18	0.09

[a] S_{BET}: BET surface area; S_{micro}: *t*-plot micropore surface area; $S_{ext} = S_{BET} - S_{micro}$. [b] V_{total}: total pore volume determined from the adsorbed volume at $P/P_0 = 0.99$; V_{micro}: *t*-plot micropore volume; $V_{meso} = V_{total} - V_{micro}$.

To investigate the local atomic environments of the samples, ^{29}Si and ^{27}Al MAS NMR spectra of the as-synthesized MOR zeolites are recorded and presented in Fig. 2. All the ^{27}Al MAS

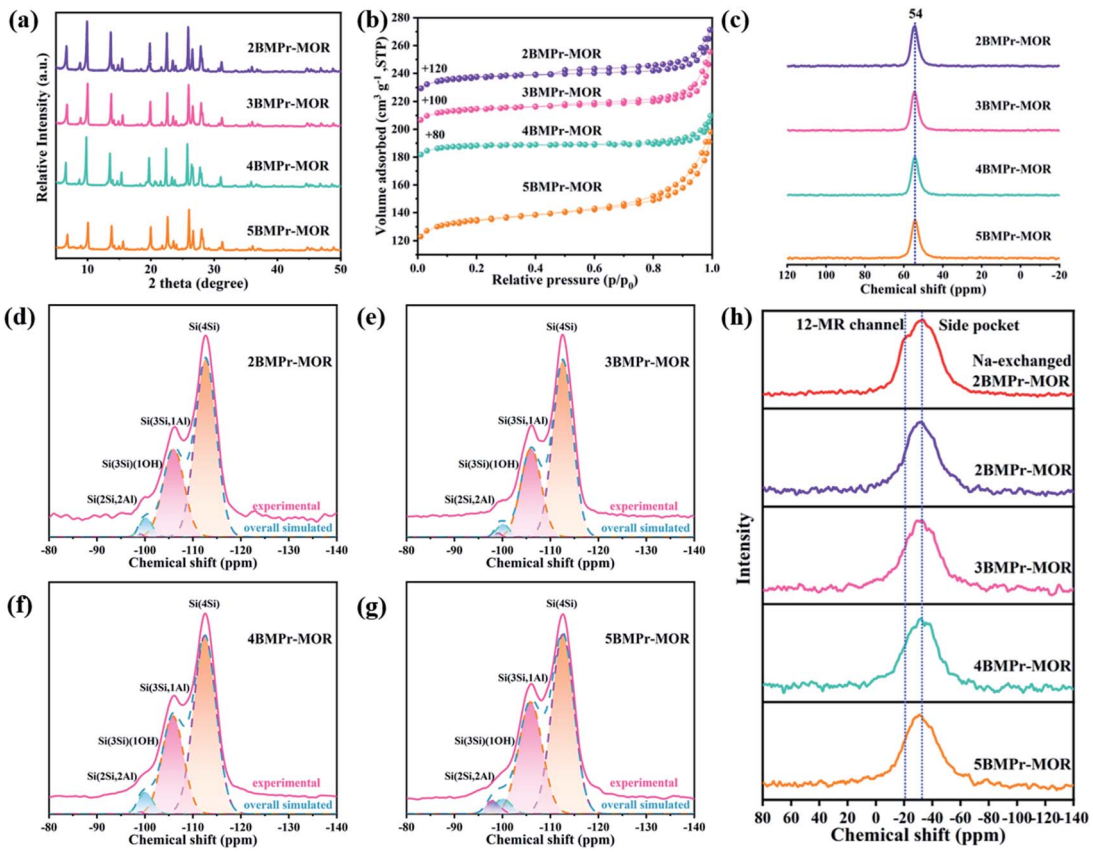

Fig. 2 (a) XRD patterns of the as-synthesized samples. (b) N_2 sorption isotherms (offset by given values) of H-MOR. (c) ^{27}Al MAS NMR spectra and (d–g) ^{29}Si MAS NMR spectra of the as-synthesized samples. (h) ^{23}Na MAS NMR spectra of the as-synthesized samples and Na-exchanged MOR sample.

Table 2 Elemental compositions, unit cell compositions and OSDA charge utilization of the MOR samples

Sample	Si/Al[a]	Na/Al[a]	C/N[a]	OSDA content[b] (wt%)	Unit cell composition[c]	N_{OSDA}/Al^{d}	U[e]
2BMPr-MOR	12.0 (12.4)	0.59	6.50	8.4 (8.0)	$Na_{2.19}[C_{12}H_{26}N_2]_{1.32}[Si_{44.30}Al_{3.70}O_{96}]$	0.41	57.2%
3BMPr-MOR	11.9 (12.0)	0.63	5.94	6.7 (6.4)	$Na_{2.34}[C_{13}H_{28}N_2]_{0.97}[Si_{44.28}Al_{3.72}O_{96}]$	0.37	71.1%
4BMPr-MOR	12.1 (12.0)	0.63	7.03	7.4 (7.4)	$Na_{2.30}[C_{14}H_{30}N_2]_{1.06}[Si_{44.35}Al_{3.65}O_{96}]$	0.37	63.7%
5BMPr-MOR	9.6 (9.4)	0.57	7.15	9.9 (10.1)	$Na_{2.59}[C_{15}H_{32}N_2]_{1.40}[Si_{43.45}Al_{4.55}O_{96}]$	0.43	70.0%
TEAOH-MOR	12.1	0.71	7.12	8.8 (8.3)	$Na_{2.58}[C_8H_{20}N]_{2.10}[Si_{44.36}Al_{3.64}O_{96}]$	0.29	50.4%

[a] Molar ratio. Si/Al and Na/Al were derived from XRF, while C/N was derived from CHN analysis. The Si/Al values in brackets were calculated from ^{29}Si MAS NMR. [b] The OSDA content was calculated from CHN analysis. The values in brackets were derived from TG analysis. [c] H_2O molecules were not included in the unit cell composition. [d] N_{OSDA}: the charges from OSDAs used for balancing the negative framework. $N_{OSDA}/Al = 1 - Na/Al$. [e] The charge utilization of *n*BMPr. $U = (n\text{Al} - n\text{Na})/2n(\text{OSDA})$, where *n*Al, *n*Na and *n*(OSDA) refer to the number of moles of Na, Al and OSDA in the unit cell composition, respectively. For TEAOH, $U = (n\text{Al} - n\text{Na})/n(\text{OSDA})$.

NMR spectra (Fig. 2c) exhibit only one symmetrical resonance at 54 ppm, corresponding to tetra-coordinated Al species, implying that all the Al species are incorporated into the framework. In the ^{29}Si MAS NMR spectra (Fig. 2d–g), the resonances at −112 ppm, −106 ppm and −99 ppm are ascribed to Si(4Si), Si(3Si,1Al), and Si(2Si,2Al) species,[29,30] respectively. The shoulder peak at around −100 ppm is speculated to be due to the existence of small amounts of silanol species (Si(3Si)(1OH) species). This assignment is further confirmed by ^{1}H–^{29}Si CP MAS NMR spectra (Fig. S4†), showing an obvious increase of the signal at −100 ppm after ^{1}H–^{29}Si cross-polarization. Based on the deconvoluted results of the ^{29}Si MAS NMR spectra, the framework SARs of the investigated samples were calculated (listed in Table 2), and were close to the bulk SARs derived from XRF.

The ^{23}Na MAS NMR spectra were measured to learn the distribution of Na^+ in the as-synthesized zeolites (Fig. 2h). According to previous literature,[31,32] the ^{23}Na MAS NMR spectra of dehydrated Na-MOR can be deconvoluted into two bands, *i.e.*, a low-field band due to Na^+ located in the 12-MR channels and a high-field band corresponding to Na^+ in the 8-MR side pockets. However, only one symmetrical high-field resonance at −32 ppm could be observed for the four as-synthesized samples, suggesting the preferential location of Na^+ in the side pockets. This is reasonable as the side pockets are the energetically favorable loci for Na^+ cations.[33,34] The absence of obvious existence of Na^+ in the 12-MR channels implies that the negative frameworks therein should be mainly counterbalanced by the bulkier OSDAs. To verify this conjecture, Na-type 2BMPr-MOR with complete Na^+ exchange was used for ^{23}Na MAS NMR measurement. As expected, one additional low-field shoulder band at *ca.* −20 ppm associated with the Na^+ in 12-MR main channels can be observed in the spectrum. These results demonstrate that Na^+ cations are preferentially located in the 8-MR side pockets during the crystallization of MOR zeolite, while *n*BMPrs tend to reside in the 12-MR channels. However, due to the second-order anisotropic broadening of ^{23}Na MAS NMR spectra, it is not possible to quantify the detailed Na^+ distribution.

The status of the encapsulated OSDAs in the as-synthesized zeolites

The status of the OSDAs in the as-synthesized samples was investigated by combined techniques including CHN analysis, TG-DSC measurement and solid state ^{1}H–^{13}C CP MAS NMR.

As shown in Table 2, the C/N molar ratios (derived from CHN analysis) of the samples are close to the theoretical values of the OSDAs, suggesting their intactness in the samples. This is further corroborated by the ^{1}H–^{13}C CP MAS NMR spectra of the as-synthesized samples (Fig. 3). The peaks in the spectra correspond well with the liquid ^{13}C NMR spectra of pure nBMPrs. Moreover, resonance splitting could be observed for the as-synthesized *n*BMPr-MOR (n = 2, 3, 4). Specifically, the resonances due to C1 atoms in the liquid ^{13}C NMR spectra are split into two peaks. Besides C1 atoms, the resonances due to C3 atoms in the methyl groups linked to N atoms are also observed to be split. Take sample 4BMPr-MOR for instance, in which the C3 resonance was split into two peaks at 52.7 and 54.9 ppm. The splitting of resonance signals was previously attributed to the different geometrical constraints and the consequently distinct van der Waals interactions between the zeolite framework and the corresponding carbon atoms. Considering the fact that the signal splitting is all associated with the carbons linked with N

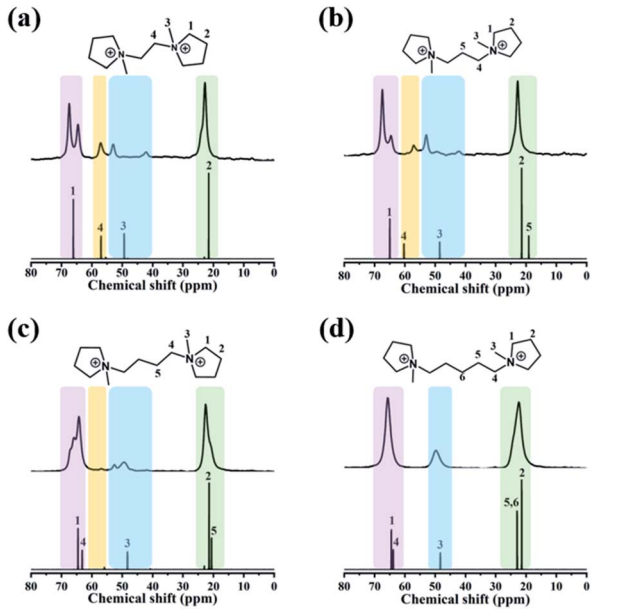

Fig. 3 The ^{1}H–^{13}C CP MAS NMR spectra (top) of the as-synthesized samples and the ^{13}C NMR spectra (bottom) of the four organic dications dissolved in D_2O.

atoms, it is speculated that the contribution of heterogeneous environments of N atoms should not be neglected.

Fig. S5† displays the TGA-DSC curves of the as-synthesized samples. Typical three-stage weight loss curves were observed for all the samples. The first weight loss stage (T < 250 °C) is unambiguously ascribed to the removal of water, accompanied by an endothermic process. The removal of the encapsulated OSDAs is further implemented in two steps. The first step in the temperature range of 250–550 °C is due to the preliminary combustion of OSDAs, which is followed by further removal of heavier residues with the increase of temperature (550–700 °C). The occluded organic content varies from 6 wt% to 10 wt% among the samples (Table 2), in agreement with CHN elemental analyses. It should be noted that no obvious weight loss or heat flow change ascribed to framework collapse could be discerned up to 900 °C, suggesting the good thermal stability of the samples.

Based on the results of thermal analysis, elemental compositions and topological structure of MOR zeolite, the unit cell compositions of the samples were derived and are listed in Table 2. It is generally acknowledged that each Na^+ can counterbalance one $[AlO_4]^-$, whereas the charge-balancing function of the N atoms is affected by the configuration and geometry hindrance of the occluded OSDA. From the unit cell compositions, the sum of Na and N atoms is higher than that of the Al atoms, suggesting that some of the N atoms are actually not counterbalancing any framework $[AlO_4]^-$. The positive charges of these N atoms might be balanced by hydroxide groups or by the internal silanol defects in the zeolite framework. Table 2 lists the N_{OSDA}/Al ratio of the samples, where N_{OSDA} refers to the charges of OSDA cations used for balancing the negative framework. The *n*BMPr-MOR samples have N_{OSDA}/Al ratios of 0.37–0.43. For comparison, MOR synthesized with conventional TEAOH as an OSDA was used as a reference sample for characterization. Note that TEA^+ can only be located in 12-MR channels due to its large size. From Table 2, TEAOH-MOR has a much higher Na/Al ratio (0.71) and thus lower N_{OSDA}/Al ratio (0.29) and charge utilization (50.4%). These results indicate that *n*BMPr cations are more efficient than TEA^+ in balancing the negative $[AlO_4]^-$ of 12-MR channels. It is speculated that the smaller steric hindrance around the N atoms of *n*BMPr may facilitate the formation of stronger host–guest interactions, contributing to the higher charge compensation ability of *n*BMPr.

To gain further information about the status of the OSDAs and their host–guest interactions with the MOR framework, a DFT-based modelling study was further performed using the Gaussian package. The energy-minimized conformations and locations of the OSDA cations are shown in Fig. 4. Clearly, all the OSDAs are preferentially distributed within the 12-MR main channels, suggesting that the 12-MR main channels are the most energetically stable sites to accommodate these dimeric OSDAs. When the OSDA cations were manually placed in the 8-MR side pockets as the initial structure for further geometry optimization, calculation failure always occurred due to energy nonconvergence. The *N*-methylpyrrolidine rings may be hindered from entering into the 8-MR pores due to their larger kinetic diameter and rigidity. This is also in good agreement with the analysis results of ^{23}Na MAS NMR spectra. The OSDA stabilization energies are given in Table S2.† 2BMPr provides the most effective stabilization towards the MOR framework. The stabilization ability shows a decreasing order of 2BMPr > 3BMPr > 4BMPr > 5BMPr, consistent with the structure-directing ability orders observed in the synthesis section.

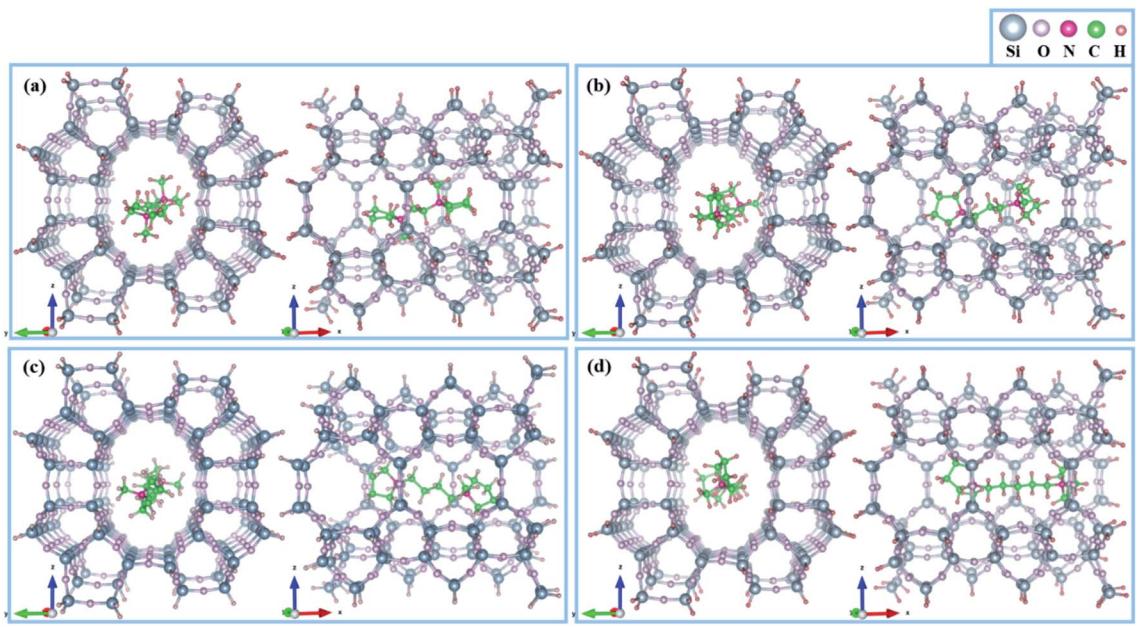

Fig. 4 Two views of the locations of four OSDAs in the most stable configurations. (a) 2BMPr-MOR, (b) 3BMPr-MOR, (c) 4BMPr-MOR, (d) 5BMPr-MOR; (left) view along the 12-MR channels; (right) view along the 8-MR connecting the side pockets and the 12-MR channels.

The acid properties of the H-MOR samples

The *n*BMPr-MOR samples with similar SARs were selected for acidity characterization, including NH_3-TPD and FTIR spectroscopy. In addition, the acid properties of the TEAOH-MOR reference sample are also investigated. As shown in Fig. 5a, all the NH_3-TPD profiles consist of two desorption peaks. The low-temperature peaks centered around 195 °C are attributed to weakly bonded NH_3 on the weak acid sites. The high-temperature peaks, which could be deconvoluted into two independent peaks, correspond to NH_3 desorption from moderate and strong acid sites. It is interesting to note that *n*BMPr-MOR samples exhibit obviously higher NH_3 desorption temperature (552–560 °C) than TEAOH-MOR (538 °C), which implies the stronger acid strength of *n*BMPr-MOR, especially 2BMPr-MOR.

The FTIR spectra in the hydroxyl vibration region are shown in Fig. 5b. The bands at 3740 cm^{-1} and 3660 cm^{-1} correspond to external isolated silanol and extra-framework aluminols, respectively.[35] The most prominent absorption band at 3606 cm^{-1}, with an obvious asymmetrical shape, is due to the acid hydroxyl groups. Actually, the band could be deconvoluted into two subbands at 3612 cm^{-1} and 3590 cm^{-1}, corresponding to the acid hydroxyls in 12-MR channels and 8-MR side pockets, respectively.[29,36–39] Deconvolution analysis (Fig. 5c) reveals that relative to the TEAOH-MOR reference sample, the proportion of BASs located in the pockets of *n*BMPr-MOR is evidently enriched. Notably, the highest 8-MR BAS proportion (67%) is observed for the MOR templated by 2BMPr. Likely, the preferential siting of Na^+ in the 8-MR side pockets of *n*BMPr-MOR, as discussed above, leads to its high BAS distribution in the side pockets.[17] In contrast, for TEAOH-MOR, it is speculated that the larger steric hindrance around the N atoms of TEA^+ causes its relatively low charge compensation ability for framework $[AlO_4]^-$, and thus necessitates the presence of Na^+ cations in the 12-MR main channels to increase the stability of the system. This speculation is consistent with the higher Na/Al ratio of TEAOH-MOR (0.71). The co-existence of Na^+ increases the charge density and consequently the Al concentration inside the 12-MR main channels, and hence its discounted BAS distribution in the side pockets. More research on the difference between *n*BMPr-MOR and TEAOH-MOR needs to be done.

NH_3-FTIR was carried out to distinguish and quantify the total BASs of the samples (Fig. S6† and Table 3). As evidenced from the hydroxyl stretching region of the spectra, the absorption bands corresponding to BAS hydroxyls completely disappear upon NH_3 adsorption, suggesting that all the acid sites could be completely titrated. Meanwhile, two new bands at

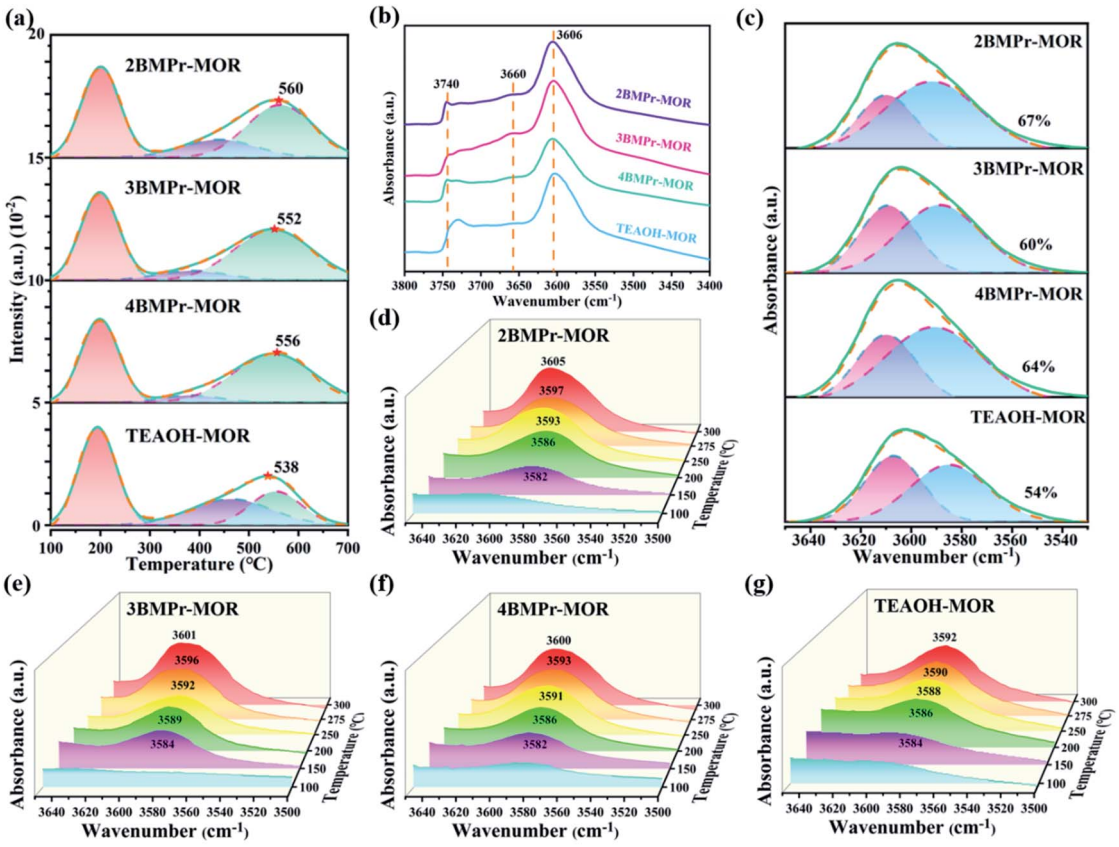

Fig. 5 (a) NH_3-TPD profiles (solid lines) and deconvoluted results (dotted lines) of the H-MOR samples. (b) FTIR spectra in the ν(OH) vibration region of the H-MOR samples. (c) Deconvoluted bands corresponding to the acid hydroxyls in the 12-MR channels (HF) and the side pockets (LF). The values refer to the proportion of BASs in the side pockets. (d–g) FTIR spectra of the ν(OH) bands after pyridine desorption at different temperatures.

Table 3 Acid amounts and BAS distribution in different channels of the H-MOR samples

	Acid amount[a] (mmol g^{-1})		BAS distribution (%)	BAS amount[b] (mmol g^{-1})	
Sample	BASs	LASs	8-MR/12-MR	8-MR	12-MR
2BMPr-MOR	0.83	0.09	67/33	0.56	0.27
3BMPr-MOR	0.73	0.23	60/40	0.43	0.30
4BMPr-MOR	0.72	0.18	64/36	0.46	0.26
TEAOH-MOR	0.74	0.07	54/46	0.40	0.34

[a] Total BASs from NH_3-FTIR based on the spectra after NH_3 desorption at 125 °C. [b] The amount of BASs in different channels of H-MOR is calculated by multiplying the distribution proportion of BASs obtained by FTIR and the total BAS amount.

1440 cm^{-1} and 1620 cm^{-1} emerge, corresponding to the NH_3 bound to the BASs and Lewis acid sites (LASs), respectively. With the rise of desorption temperature, the acid hydroxyls of high frequency (HF) were firstly recovered, and then gradually moved to lower frequency (LF), indicating the stronger acidity of low-frequency (LF) acid hydroxyls in the side pockets. This implies that the stronger acidities of *n*BMPr-MOR as revealed by NH_3-TPD should originate from their enriched BAS distributions in the 8-MR side pockets.

The concentrations of the BASs located in the 8-MR and 12-MR channels were further calculated, and the corresponding results are included in Table 3. 2BMPr-MOR possesses the largest 8-MR BAS amount (0.56 mmol g^{-1}), while TEAOH-MOR has the lowest value (0.40 mmol g^{-1}). The detailed order is as follows: 2BMPr-MOR > 4BMPr-MOR > 3BMPr-MOR > TEAOH-MOR. Such an order is in good agreement with the acid strength revealed by NH_3-TPD, as the acid sites in 8-MR have been demonstrated to have higher acid strength than those in 12-MR. The large BAS amounts in 8-MR of *n*BMPr-MOR are expected to be favorable for their catalytic application in the DME carbonylation reaction.

Catalytic performance for DME carbonylation

The catalytic performance of *n*BMPr-MOR with similar SARs was evaluated in the DME carbonylation reaction. For comparison, TEAOH-MOR was tested as a reference catalyst. Before the reaction, pyridine modification on the catalysts was carried out to mitigate the occurrence of MTH side reactions.[40] Fig. 5d–g indicate the pyridine desorption behavior over the samples. It can be found that pyridine in the 8-MR side pockets is preferentially desorbed,[41] as evidenced by the gradual shift of exposed hydroxyls to higher frequency (from 3582 to 3605 cm^{-1}). At a desorption temperature of 275 °C, the exposed BASs of the 8-MR pockets reach the maximum, accompanied by a slight exposure of BASs in the 12-MR channels. Thus, the pyridine desorption temperature of the catalysts was decided to be 275 °C for the present investigation.

Fig. 6a and S7† illustrate the time-dependent evolution of DME conversion and MeOAc selectivity of the samples. An induction period could be observed for all the investigated samples, which is due to the establishment of surface methoxy

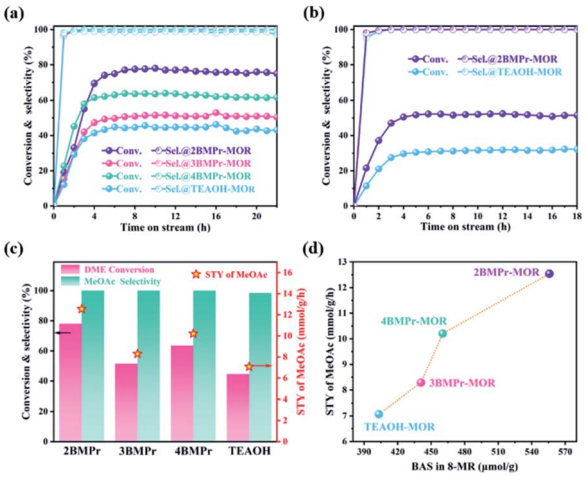

Fig. 6 (a and b) DME conversion and MeOAc selectivity as a function of time during DME carbonylation over pyridine-modified H-MOR catalysts. Reaction conditions: 200 °C, 2 MPa, DME/CO/N_2 = 5/35/60, GHSV = 7200 mL g^{-1} h^{-1} (for a) or 12 000 mL g^{-1} h^{-1} (for b). (c) DME conversion, MeOAc selectivity and space-time yield at TOS = 10 h. (d) Correlation of STY of MeOAc and BAS amount in 8-MR side pockets.

species and the accompanied release of methanol and H_2O molecules.[42] Following the coverage of the BASs on the catalysts, both the DME conversion and MeOAc selectivity rise gradually and reach their steady state. The steady-state MeOAc selectivity on all catalysts is higher than 99%. In addition, a clear DME carbonylation activity variance could be observed among the samples. The highest steady-state DME conversion (78%) was achieved on 2BMPr-MOR. Even under high GHSV conditions (Fig. 6b), 2BMPr-MOR still showed superior carbonylation activity as compared to TEAOH-MOR, which corresponds well with its highest BAS quantity inside the side pockets. As for 3BMPr-MOR and 4BMPr-MOR, they exhibit medium activity between 2BMPr-MOR and TEAOH-MOR. As our previous studies have evidenced the excellent catalytic performance of TEAOH-MOR,[9] herein the obviously higher conversions on *n*BMPr-MOR (n = 2–4) imply that they are highly efficient catalysts for DME carbonylation. The space-time yield (STY) of MeOAc on the samples was calculated and is given in Fig. 6c and d. It can be found that the STY of MeOAc has a positive correlation with the 8-MR BAS amount of the samples, but they do not show a good linear relationship. This is understandable as previous studies have revealed that the catalytic activity of the BASs in side pockets is inhomogeneous.[9] Moreover, it is noted that the STY of MeOAc on 2BMPr-MOR reaches as high as 12.5 mmol g^{-1} h^{-1}. To the best of our knowledge, this is the highest value ever reported for DME carbonylation using zeolitic catalysts under similar test conditions (Table S3†).

Conclusion

A series of MOR zeolites were successfully prepared by the employment of bulky gemini-type bis(methylpyrrolidinium) dications as novel OSDAs. It was demonstrated that the structure directing ability of nBMPr increased following the

shortening of methylene chain lengths, and the *n*BMPr cations located in the 12-MR channels of the resultant materials. In comparison with the TEAOH-MOR reference sample, *n*BMPr-MOR (especially 2BMPr-MOR) possessed obviously enhanced acid strength and BAS distribution/amounts in the 8-MR side pockets. The reason for such a phenomenon should lie in the higher charge balancing ability of *n*BMPr cations for the framework $[AlO_4]^-$ of 12-MR channels, which promotes the preferential siting of Na^+ in the side pockets and thus the improved 8-MR BAS distribution. Consequently, *n*BMPr-MOR exhibited superior DME carbonylation activity with STY of MeOAc as high as 12.5 mmol g^{-1} h^{-1}. The present study implies that the acid distributions in MOR zeolite could be tailored by designed OSDAs with varied steric hindrance and charge density, which would contribute to the further improvement of zeolite catalysts.

Conflicts of interest

There are no conflicts to declare.

Acknowledgements

This work was supported by the Key Research Program of Frontier Sciences, Chinese Academy of Sciences (Grant No. QYZDB-SSW-JSC040), the National Natural Science Foundation of China (No. 21991090 and 21991091), and funding from the Sino-French International Laboratory (LIA) "Zeolites".

Notes and references

1 A. Corma, *Chem. Rev.*, 1997, **97**, 2373–2419.
2 C. S. Cundy and P. A. Cox, *Chem. Rev.*, 2003, **103**, 663–702.
3 P. Tian, Y. Wei, M. Ye and Z. Liu, *ACS Catal.*, 2015, **5**, 1922–1938.
4 H. Gies and B. Marler, *Zeolites*, 1992, **12**, 42–49.
5 A. A. C. Reule and N. Semagina, *ACS Catal.*, 2016, **6**, 4972–4975.
6 D. B. Rasmussen, J. M. Christensen, B. Temel, F. Studt, P. G. Moses, J. Rossmeisl, A. Riisager and A. D. Jensen, *Angew. Chem., Int. Ed.*, 2015, **54**, 7261–7264.
7 P. Cheung, A. Bhan, G. J. Sunley and E. Iglesia, *Angew. Chem., Int. Ed.*, 2006, **45**, 1617–1620.
8 L. Li, Q. Wang, H. Liu, T. Sun, D. Fan, M. Yang, P. Tian and Z. Liu, *ACS Appl. Mater. Interfaces*, 2018, **10**, 32239–32246.
9 K. Cao, D. Fan, L. Li, B. Fan, L. Wang, D. Zhu, Q. Wang, P. Tian and Z. Liu, *ACS Catal.*, 2020, **10**, 3372–3380.
10 L. Wang, H. Xu, N. Yan, S. Correll, S. Xu, P. Guo, P. Tian and Z. Liu, *CrystEngComm*, 2018, **20**, 699–702.
11 P. Wang, L. Huang, J. Li, M. Dong, J. Wang, T. Tatsumi and W. Fan, *RSC Adv.*, 2015, **5**, 28794–28802.
12 B. C. Knott, C. T. Nimlos, D. J. Robichaud, M. R. Nimlos, S. Kim and R. Gounder, *ACS Catal.*, 2018, **8**, 770–784.
13 W. Chu, X. Liu, Z. Yang, H. Nakata, X. Tan, X. Liu, L. Xu, P. Guo, X. Li and X. Zhu, *Chin. J. Catal.*, 2021, **42**, 2078–2087.
14 Y. Yuan, L. Wang, H. Liu, P. Tian, M. Yang, S. Xu and Z. Liu, *Chin. J. Catal.*, 2015, **36**, 1910–1919.
15 M.-N. Liu, Y.-Z. Li, Z.-X. Xie, Q.-Q. Hao, Q.-X. Luo, J. Zhang, H. Chen, C. Dai and X. Ma, *New J. Chem.*, 2020, **44**, 16638–16644.
16 M. Ma, X. Huang, E. Zhan, Y. Zhou, H. Xue and W. Shen, *J. Mater. Chem. A*, 2017, **5**, 8887–8891.
17 Y. Li, M. Yu, K. Cai, M. Wang, J. Lv, R. F. Howe, S. Huang and X. Ma, *Phys. Chem. Chem. Phys.*, 2020, **22**, 11374–11381.
18 K. Lu, J. Huang, L. Ren, C. Li, Y. Guan, B. Hu, H. Xu, J. Jiang, Y. Ma and P. Wu, *Angew. Chem., Int. Ed.*, 2020, **59**, 6258–6262.
19 Y. Li, S. Huang, Z. Cheng, K. Cai, L. Li, E. Milan, J. Lv, Y. Wang, Q. Sun and X. Ma, *Appl. Catal., B*, 2019, **256**, 117777.
20 M. Moliner, J. González, M. T. Portilla, T. Willhammar, F. Rey, F. J. Llopis, X. Zou and A. Corma, *J. Am. Chem. Soc.*, 2011, **133**, 9497–9505.
21 C. Baerlocher, F. Gramm, L. Massueger, L. B. McCusker, Z. He, S. Hovmoeller and X. Zou, *Science*, 2007, **315**, 1113–1116.
22 X. Hong, W. Chen, G. Q. Zhang, Q. M. Wu, C. Lei, Q. Y. Zhu, X. J. Meng, S. C. Han, A. M. Zheng, Y. H. Ma, A. N. Paryulescu, U. Muller, W. P. Zhang, T. Yokoi, X. H. Bao, B. Marler, D. E. De Vos, U. Kolb and F. S. Xiao, *J. Am. Chem. Soc.*, 2019, **141**, 18318–18324.
23 S. B. Hong, H.-K. Min, C.-H. Shin, P. A. Cox, S. J. Warrender and P. A. Wright, *J. Am. Chem. Soc.*, 2007, **129**, 10870–10885.
24 J. Datka, B. Gil and A. Kubacka, *Zeolites*, 1995, **15**, 501–506.
25 M. Frisch, G. Trucks, H. Schlegel, G. Scuseria, M. Robb, J. Cheeseman, G. Scalmani, V. Barone, B. Mennucci and G. Petersson, *Gaussian 09, Revision B.01*, Gaussian, Inc., Wallingford CT, 2009.
26 D. Lesthaeghe, B. De Sterck, V. Van Speybroeck, G. B. Marin and M. Waroquier, *Angew. Chem., Int. Ed.*, 2007, **46**, 1311–1314.
27 D. K. Papayannis, K. D. Papavasileiou and V. S. Melissas, *Microporous Mesoporous Mater.*, 2016, **226**, 1–9.
28 J. D. Chai and M. Head-Gordon, *Phys. Chem. Chem. Phys.*, 2008, **10**, 6615–6620.
29 H. Xue, X. Huang, E. Zhan, M. Ma and W. Shen, *Catal. Commun.*, 2013, **37**, 75–79.
30 J. Yao, X. Feng, J. Fan, Y. He, R. Kosol, Y. Zeng, G. Liu, Q. Ma, G. Yang and N. Tsubaki, *Microporous Mesoporous Mater.*, 2020, **306**, 110431.
31 M. Hunger, P. Sarv and A. Samoson, *Solid State Nucl. Magn. Reson.*, 1997, **9**, 115–120.
32 K. Cao, D. Fan, S. Zeng, B. Fan, N. Chen, M. Gao, D. Zhu, L. Wang, P. Tian and Z. Liu, *Chin. J. Catal.*, 2021, **42**, 1468–1477.
33 M. Hunger, P. Sarv and A. Samoson, *Solid State Nucl. Magn. Reson.*, 1997, **9**, 115–120.
34 V. D. Dominguez-Soria, P. Calaminici and A. Goursot, *J. Chem. Phys.*, 2007, **127**, 154710.
35 M. Maache, A. Janin, J. C. Lavalley and E. Benazzi, *Zeolites*, 1995, **15**, 507–516.
36 V. L. Zholobenko, M. A. Makarova and J. Dwyer, *J. Phys. Chem.*, 1993, **97**, 5962–5964.
37 F. Wakabayashi, J. Kondo, A. Wada, K. Domen and C. Hirose, *J. Phys. Chem.*, 1993, **97**, 10761–10768.

38 Y. Li, Q. Sun, S. Huang, Z. Cheng, K. Cai, J. Lv and X. Ma, *Catal. Today*, 2018, **311**, 81–88.
39 X. Wang, R. Li, C. Yu, Y. Liu, L. Zhang, C. Xu and H. Zhou, *Fuel*, 2019, **239**, 794–803.
40 J. Liu, H. Xue, X. Huang, P.-H. Wu, S.-J. Huang, S.-B. Liu and W. Shen, *Chin. J. Catal.*, 2010, **31**, 729–738.
41 D. B. Lukyanov, T. Vazhnova, N. Cherkasov, J. L. Casci and J. J. Birtill, *J. Phys. Chem. C*, 2014, **118**, 23918–23929.
42 P. Cheung, A. Bhan, G. J. Sunley, D. J. Law and E. Iglesia, *J. Catal.*, 2007, **245**, 110–123.